Simple synthesis of platinum–palladium nanoflowers on reduced graphene oxide and their enhanced catalytic activity for oxygen reduction reaction

Jing-Jing Lv, Jie-Ning Zheng, Hong-Bao Zhang, Meng Lin, Ai-Jun Wang[*], Jian-Rong Chen, Jiu-Ju Feng[*]

College of Geography and Environmental Science, College of Chemistry and Life Science, Zhejiang Normal University, Jinhua 321004, China

HIGHLIGHTS

- Well-defined Pt–Pd nanoflowers supported on RGOs are prepared by a facile wet-chemical strategy.
- This approach is simple, without any seed, template, organic solvent, or special apparatus.
- $NaNO_2$ and PVP are essential to the formation of flower-like Pt–Pd nanostructures.
- The nanocomposites display the enhanced electrocatalytic activity and long-term stability for ORR.

GRAPHICAL ABSTRACT
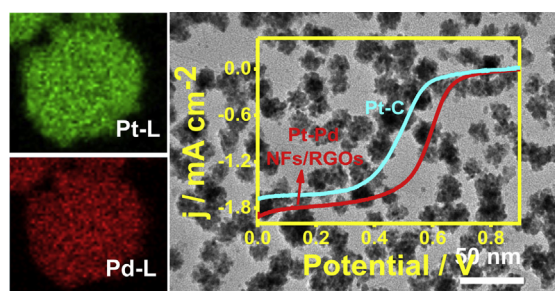
ABSTRACT

A simple and rapid one-pot wet-chemical method is developed for large-scale preparation of reduced graphene oxide nanosheets supporting Pt–Pd nanoflowers (Pt–Pd NFs/RGOs) using hydrazine hydrate as a reducing agent, without any seed, template, organic solvent, or special apparatus. The coexistence of sodium nitrite ($NaNO_2$) and poly(vinyl pyrrolidone) (PVP), and their amounts are essential for synthesis of flower-like nanostructures. Besides, Pt–Pd NFs/RGOs have higher catalytic activity and better durability for oxygen reduction reaction, compared with commercial Pt–C (50 wt %).

© 2014 Elsevier B.V. All rights reserved.

1. Introduction

Currently, Pt-based catalysts have been widely used as the best active catalytic components for direct alcohol fuel cells [1–3]. Nevertheless, their commercialization is severely limited by many drawbacks such as the high price and limited reserves of Pt [4].

Moreover, Pt-based catalysts confront the sluggish kinetics, which can seriously degrade the efficiency of fuel cells [5]. Additionally, their catalytic activity gradually decreases, because the generated carbonaceous intermediate species tend to cover the surface active sites by chemical adsorption [6]. Thus, it is still a great challenge to improve their catalytic performances and search alternatives, while reduce the content of Pt for practical applications.

Alloying Pt with a second metal (M = Pd, Ni, Ag, and Cu) is a promising approach to reduce the dosage of Pt and enhance the catalytic performance. To date, several successful examples have

* Corresponding authors. Tel./fax: +86 579 82282269.
E-mail addresses: ajwang@zjnu.cn, ajwangnju@gmail.com (A.-J. Wang), jjfeng@zjnu.cn (J.-J. Feng).

been reported for bimetallic alloys [7–10]. Another effective strategy is to decrease the size of Pt-based catalysts, which can be possible by enhancing specific surface areas per mass or using supporting materials with high surface areas [11–13].

It is known that graphene as one of carbon-based nanomaterials has attracted enormous interest for its unique features, including the large surface area, good electrical conductivity, great mechanical strength, and abundant functional groups on the surface [14,15]. As a result, graphene is extensively selected as an attractive support for loading electrocatalysts, mainly owing to its fast 2D electron-transfer kinetics [16]. Up to now, several methods have been developed to synthesize Pt-based alloys supported on (reduced) graphene oxide nanosheets ((R)GOs) [17,18]. However, the synthesis methods are complex and time-consuming. For example, Liu and co-workers synthesized PdAg nanorings supported on graphene nanosheets based on galvanic displacement reaction between pre-synthesized Ag nanoparticles and Pd^{2+} ions [19]. Li et al. prepared AuPd nanoparticles dispersed on RGOs by a hydrothermal method [20]. It is still required to explore simple, reliable, and green synthesis methods for development of Pt-based catalysts.

Herein, a simple and rapid one-pot wet-chemical strategy was designed to prepare RGOs supported Pt–Pd nanoflowers (donated as Pt–Pd NFs/RGOs) with a high yield, using hydrazine hydrate as a reducing agent, without any seed, template, organic solvent, or special apparatus. The electrocatalytic activity and stability of the as-prepared nanocomposites were investigated, using oxygen reduction reaction (ORR) as a model system.

2. Experimental section

2.1. Chemicals

Chloroplatinic acid (H_2PtCl_6), palladium chloride ($PdCl_2$), poly(vinyl pyrrolidone) (PVP, MW = 58 000), $NaNO_2$, and hydrazine hydrate (80 wt %) were purchased from Shanghai Aladdin Chemical Reagent Company (Shanghai, China). Commercial Pt–C (50 wt %) was bought from Alfa Aesar Chemicals company (China, Shanghai). All the other chemicals were analytical grade and used without further purification. All aqueous solutions were prepared with twice-distilled water.

2.2. Synthesis of Pt–Pd NFs/RGOs

For typical synthesis of Pt–Pd NFs/RGOs, GOs were firstly prepared by the modified Hummer's method [21]. Next, 0.5 mL of 100 mM $PdCl_2$, 1.29 mL of 38.62 mM H_2PtCl_6, and 17.3 mg $NaNO_2$ were put into a 10 mL PVP solution (0.25 wt %) containing 0.2 mg mL^{-1} GOs under stirring. Afterward, the pH of the mixed solution was adjusted to 12 with freshly prepared 0.1 M NaOH. Next, the mixture was placed into the ice-bath and quickly turned black upon the addition of 100 μL hydrazine hydrate (80 wt %) under stirring. The black solution was further stirred for another 30 min under the ice-bath. Finally, the black precipitate was collected by centrifugation, thoroughly washed with ethanol and water to remove the residual PVP, and dried at 60 °C in a vacuum.

Control experiments were performed by adjusting the amount of PVP and $NaNO_2$, along with varying different reductants, while other conditions were kept unchanged.

2.3. Instrumentation

The morphology and composition of the samples were characterized by transmission electron microscopy (TEM), high-resolution TEM (HRTEM) images, and high angle annular dark field-scanning transmission electron microscopy (HAADF-STEM), as well as X-ray energy dispersive spectra (EDS) on a JEM-2100F transmission electron microscope coupled with an energy-dispersive X-ray spectrometer (Oxford-1NCA). TEM analysis was carried out at an accelerating voltage of 200 kV, and Cu grids were used as substrates. The crystal structures were examined by X-ray diffraction (XRD) analysis on a Bruker-D8-AXS diffractometer system equipped with Cu Kα radiation (Bruker Co., Germany). X-ray photoelectron spectroscopy (XPS) measurements were performed by a thermofisher-ESCALab 250 (ThermoFisher, E. Grinstead, UK), using Al Kα X-ray radiation (1486.6 eV) for excitation. The UV–vis absorption spectra were recorded on a Lambda950 UV/Vis/NIR spectrometer. Raman spectra were obtained on a Renishaw Raman system model 1000 spectrometer equipped with a CCD detector. Thermogravimetric analysis (TGA) was performed in air on a NETZSCH STA 449C analyzer, where the samples were heated from 25 to 900 °C at a heating rate of 10 °C min^{-1}.

2.4. Electrochemical measurements

All electrochemical experiments were performed on a CHI 660D electrochemical workstation (CH Instruments, Chenhua Co., Shanghai, China) with a conventional three-electrode cell, including a platinum wire as counter electrode, an Ag/AgCl electrode or saturated calomel electrode (SCE) as reference electrode, and a modified glassy carbon electrode (GCE, 3.0 mm diameter) or rotating disk electrode (Model 616, RDE, 4 mm diameter) as working electrode.

For typical preparation of the modified GCE and RDE, 2 mg of Pt–Pd NFs/RGOs was dispersed into 1.0 mL of water under ultra-sonication for 30 min to obtain a homogeneous suspension (2 mg mL^{-1}). Similarly, the suspension of 0.4 mg mL^{-1} was prepared for the sample. Then, 6 μL of the 2 mg mL^{-1} suspension was placed on the GCE surface and 30 μL of the 0.4 mg mL^{-1} suspension was dropped on the RDE surface using the macrosyringe, followed by casting another layer of Nafion (0.05 wt %) on the electrode surfaces to seal the samples in place. The resulting specific loading for GCE (or RDE) was 0.1700 (or 0.0955) mg cm^{-2}. For comparison, commercial Pt–C (50 wt %) modified GCE and RDE were prepared in a similar way.

Electrochemical CO-stripping voltammograms were acquired by oxidizing pre-adsorbed CO (CO_{ad}) in 0.5 M H_2SO_4 at a scan rate of 50 mV s^{-1}. CO was purged through the electrolyte for 30 min to allow complete adsorption of CO onto the samples. The amount of the CO_{ad} was evaluated by integrating the CO_{ad} stripping peak and correcting for the capacitance of the double electric layer. The cyclic voltammetry experiments were performed in 0.5 M H_2SO_4 at a scan rate of 50 mV s^{-1}. The ORR measurements were conducted in O_2-saturated 0.5 M H_2SO_4 at a scan rate of 5 mV s^{-1}. All the experiments were carried out at room temperature, if not stated otherwise.

3. Results and discussion

As shown in Fig. 1A, the product contains large-scale flower-like nanoparticles uniformly dispersed on RGOs. The flower-like nanostructures consist of several ultrathin irregular petals (Fig. 1B and C). Their average diameter is 19.4 nm, with the narrow size distribution from 13 to 25 nm (Fig. 1B, Inset). And their high crystallization is clearly confirmed by the selected-area electron diffraction (SAED) pattern (inset in Fig. 1C) [3], as further demonstrated by the associated HRTEM images (Fig. 1D). Furthermore, the lattice d-spacing distance is around 0.23 nm, obtained at different marked regions of a single nanoflower, which is consistent with the (111) planes of the face-centered cubic (fcc) Pt–Pd alloy [22].
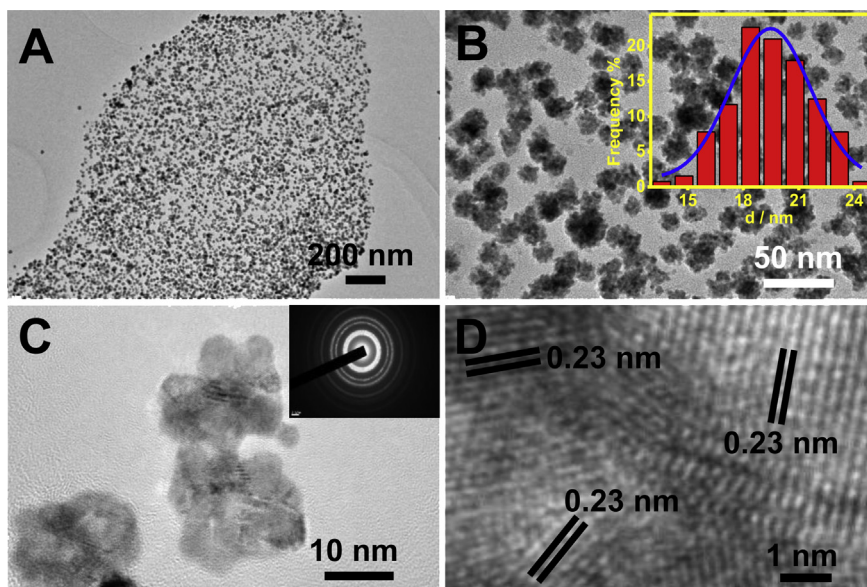
Fig. 1. Low (A), medium (B), and high magnification (C, D) TEM images of Pt–Pd NFs/RGOs. Insets show the corresponding particle size distribution (in B) and SAED pattern (in C).

HAADF-STEM-EDS mapping (Fig. 2A) and EDS line scanning profiles (Fig. 2B) reveal homogeneous distribution of both Pt and Pd elements across the whole nanoflower, as strongly verified by the EDS spectrum (Fig. 2C), showing the formation of Pt–Pd alloys [6]. In addition, the atomic ratio of Pt to Pd is about 3:2 in Pt–Pd NFs/RGOs.

Importantly, XRD spectra (Fig. 2D) were measured to further examine the composition and crystal structures of Pt–Pd NFs/RGOs (curve a), in which four representative diffraction peaks are detected at 40.1°, 46.6°, 68.3°, and 81.9°, corresponding to the (111), (200), (220) and (311) planes of the fcc Pt–Pd alloy [23]. Moreover, an extra peak is emerged at 21.4°, unlike the original GOs only with a sharp peak at 10.9° (curve b). These findings indicate complete removal of oxygen-containing groups from GOs after the reduction process, causing the formation of RGOs [24].

Raman and UV–vis spectra were commonly used to characterize the electronic and structural properties of carbon-based materials [25,26]. Fig. 3A illustrates the Raman spectra of Pt–Pd NFs/RGOs
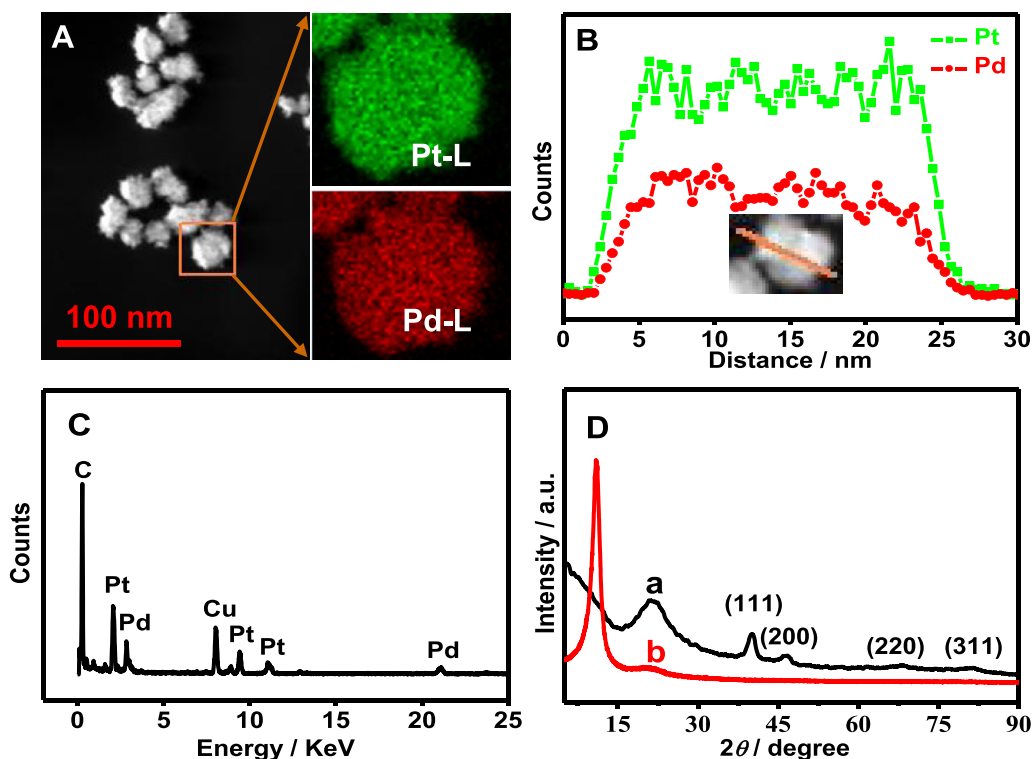

Fig. 2. HAADF-STEM-EDS mapping images (A) and EDS line scanning profiles (B), EDS (C), and XRD (D) spectra of Pt–Pd NFs/RGOs.
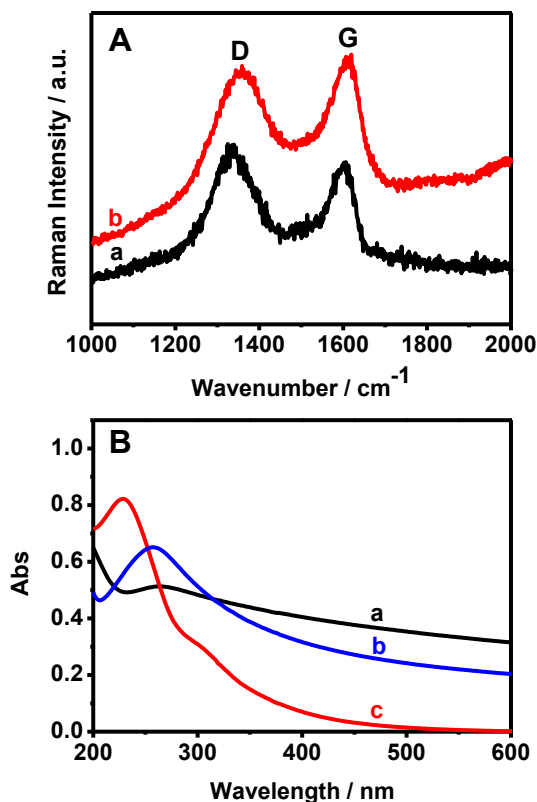
Fig. 3. Raman spectra (A) of Pt−Pd NFs/RGOs (curve a) and GOs (curve b). UV−vis spectra (B) of Pt−Pd NFs/RGOs (curve a), RGOs (curve b), and GOs (curve c).

Fig. 5. TEM images of the products synthesized with $NaBH_4$ (A) and AA (B).

(curve a) and GOs (curve b). The two typical peaks correspond to the D and G bands [27]. The D band is related to the sp^2 carbon atoms of disordered graphene nanosheets, while the G band comes from the E_{2g} mode of graphite. Thus, the intensity ratios of the two
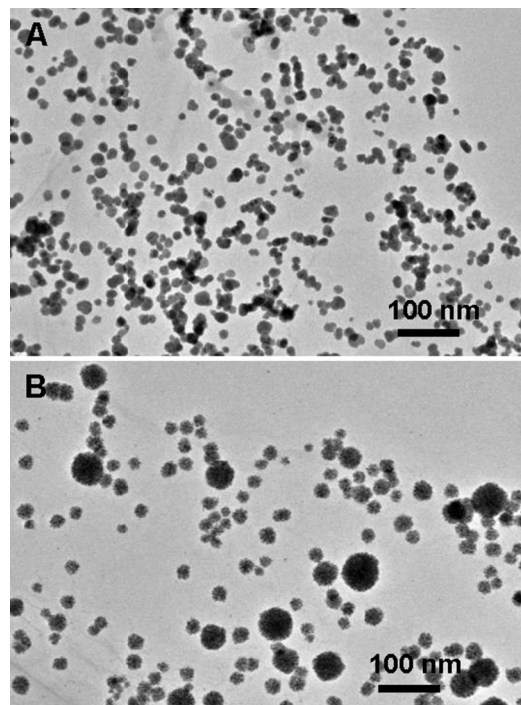
bands (I_D/I_G) are usually used to explain the chemical modification degree of the graphitic carbon samples [28]. The ratio of the I_D/I_G is 1.10 for Pt−Pd NFs/RGOs, which is larger than that of GOs (0.96), implying the decreased size of the in-plane sp^2 domains, revealing efficient reduction of GOs. This is ascribed to the introduction of a local disorder band and several defects induced by chemical reduction [29].
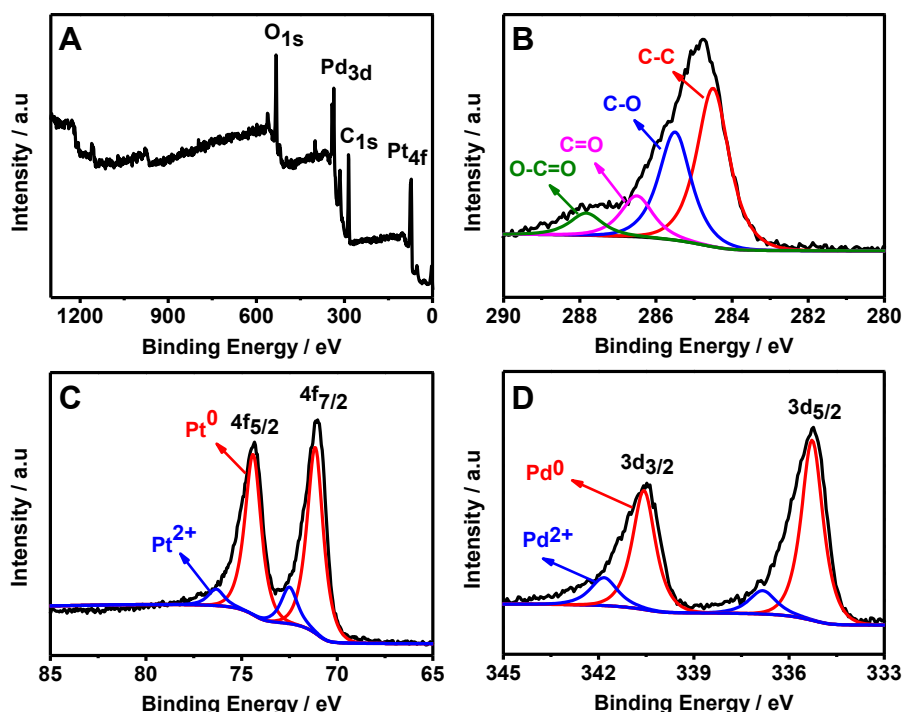

Fig. 4. Survey (A), high resolution C 1s (B), Pt 4f (C), and Pd 3d (D) XPS spectra of Pt−Pd NFs/RGOs.

Meanwhile, UV–vis spectra of Pt−Pd NFs/RGOs (Fig. 3B, curve a), RGOs (Fig. 3B, curve b), and GOs (Fig. 3B, curve c) are provided, further verifying the effective reduction of GOs to RGOs. Specifically, there is a strong absorption peak detected at 229 nm for GOs corresponding to the $\pi \rightarrow \pi^*$ transitions of the aromatic C=C bond [7]. However, this peak red shifts to 258 nm for RGOs and Pt−Pd NFs/RGOs, accompanied with the decrease of the peak intensity, convincingly proving the formation of RGOs in the present synthesis [30].

XPS analysis is utilized to determine the surface state and composition of Pt−Pd NFs/RGOs. The survey XPS spectrum reveals the product contains C, O, Pt, and Pd elements (Fig. 4A). As displayed by high-resolution C 1s XPS spectrum, the peak from the C−C bond (284.5 eV) is much stronger than those from the C−O (285.5 eV), C=O (286.5 eV), and O−C=O (287.9 eV) groups (Fig. 4B), further confirming the efficient reduction of GOs, as demonstrated by the Raman measurements [20,31]. The existence state of Pt is deciphered (Fig. 4C), in which there are two pairs of Pt 4f characteristic peaks observed. Specifically, the stronger pair (71.2 and 74.4 eV) is originated from metallic Pt^0, while the weaker couple (72.5 and 76.4 eV) is assigned to Pt^{II} specie in the forms of PtO and $Pt(OH)_2$ [32]. Estimated from the peak intensity, Pt^0 is the predominant species in Pt−Pd NFs/RGOs, revealing complete reduction of the Pt precursors [33,34]. Similar observation is made

for Pd 3d region (Fig. 4D), illustrating the main species of Pd^0 in Pt−Pd NFs/RGOs. The predominant Pt^0 and Pd^0 species are expected to improve the catalytic activity towards oxygen reduction [35]. Besides, the loading of Pt−Pd alloy in Pt−Pd NFs/RGOs is calculated to be 88 wt % based on the TGA data (Fig. S1, Supporting information) [36].

Impressively, an appropriate reducing agent is critical for synthesis of Pt−Pd NFs/RGOs. In the control experiments, a large number of spherical Pt−Pd alloy nanoparticles are produced by using sodium borohydride ($NaNH_4$) instead of hydrazine hydrate as a reducing agent (Fig. 5A), while the use of ascorbic acid (AA) induces the formation of many irregular porous nanospheres with a broad size distribution (Fig. 5B). Thus, the distinct differences in morphology are attributed to the different reaction kinetics caused by the associated reducing agent [37]. The weaker reducing ability of AA brings a slower nucleation process, but facilitates subsequent selective growth of large porous nanostructures [38]. In contrast, the stronger reducing capability of $NaBH_4$ induces rapid nucleation and instantaneously develops into spheres to minimize the surface energy of nuclei [39]. These results verify that comparatively mild reducing ability of hydrazine hydrate is essential to the formation of Pt−Pd NFs.

Most importantly, without (Fig. 6A), with insufficient (Fig. 6B), and excessive (Fig. 6C) $NaNO_2$ hardly yield flower-like nanocrystals, because of the essential role of $NaNO_2$ preferentially adsorbed on the Pt−Pd alloy surface as a structure-directing agent [40]. Meanwhile, the products are some irregular nanospheres aggregated together in the absence of PVP (Fig. S2A, Supporting information). And its less dosage (i.e. 0.1 wt % PVP, Fig. S2B, Supporting information) fails to produce Pt−Pd NFs, as obtained from the
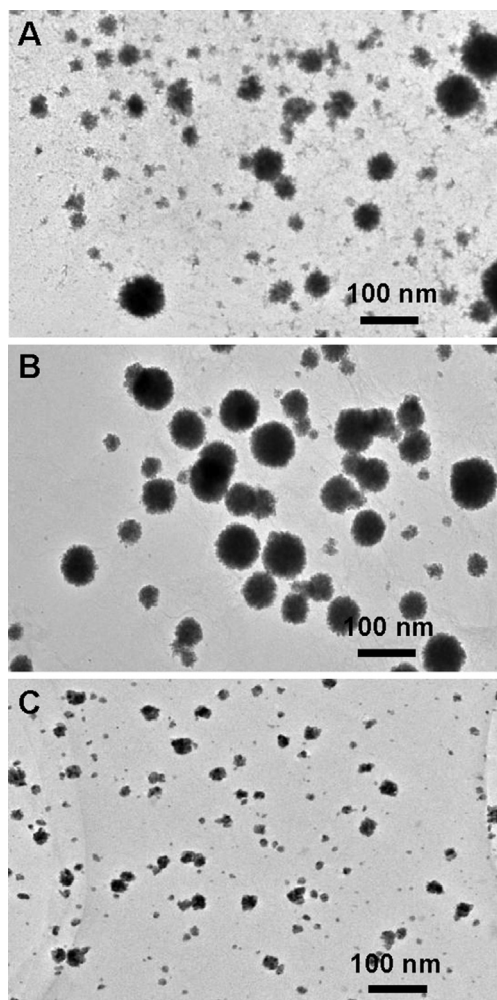

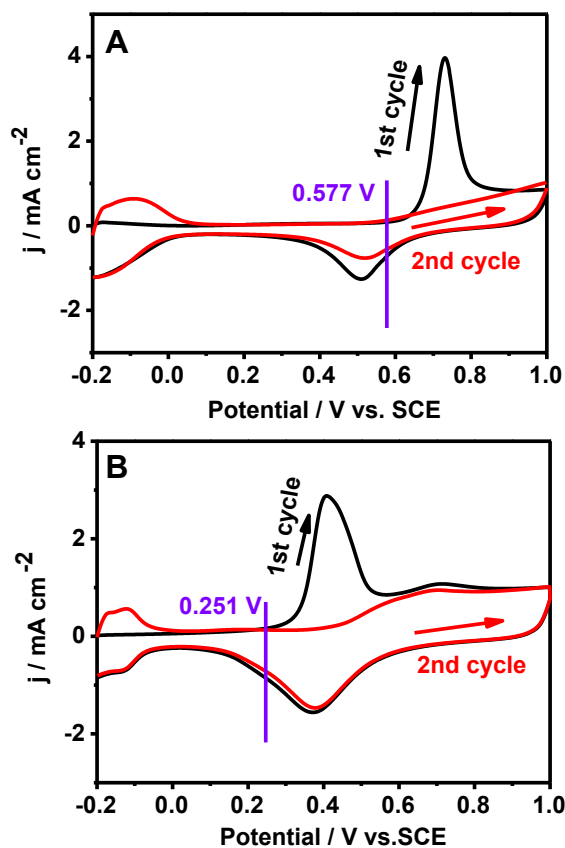**Fig. 6.** TEM images of the products obtained in the absence (A) and presence of 5 mM (B) and 50 mM (C) $NaNO_2$.

Fig. 7. CO-stripping voltammograms of the Pt−Pd NFs/RGOs (A) and commercial Pt−C (50 wt %, B) modified electrodes in 0.5 M H_2SO_4 at a scan rate of 50 mV s^{-1}.

standard procedure with 0.25 wt % PVP. Thus, the coexistence of $NaNO_2$ and PVP, along with their appropriate amounts, is extremely necessary for flower-like Pt–Pd nanostructures with high quality [41,42].

The electrochemically active surface area (EASA) of the Pt–Pd NFs/RGOs modified electrodes was calculated by the CO-stripping measurements (Fig. 7) based on the following equation [43–46]:

$$EASA \left(m^2\ g^{-1} \right) = \mathbf{Q}/\{G \times 420\}$$

Herein, Q represents the charges of CO desorption–electrooxidation, G is the Pt loading on the electrode surface, and 420 is the charges required to oxidize a monolayer of CO on bright Pt ($\mu C\ cm^{-2}$). The EASA is 15.8 $m^2\ g^{-1}$ for Pt–Pd NFs/RGOs, which is even higher than that of commercial Pt–C (50 wt %, 15.1 $m^2\ g^{-1}$). The larger EASA of Pt–Pd NFs/RGOs provides multiple active sites available for the target molecules, which imply the improved electrocatalytic activity of Pt–Pd NFs/RGOs [47,48].

The electrocatalytic activity of Pt–Pd NFs/RGOs was examined using ORR as a model system. Fig. 8A shows the polarization curves of the Pt–Pd NFs/RGOs (curve a) and commercial Pt–C (50 wt %, curve b) modified electrodes conducted in O_2-saturated 0.5 M H_2SO_4. The Pt–Pd NFs/RGOs modified electrode displays much higher diffusion-limiting current density than that of commercial Pt–C (50 wt %). Besides, the half-wave potential of Pt–Pd NFs/RGOs

is 0.62 V, which is more positive than that of commercial Pt–C (50 wt %, 0.48 V), three-dimensional dendritic Pt nano-electrocatalyst (0.57 V) [49], and mesoporous hollow PtCu nano-particles (0.51 V) [50], respectively. These results mean the improved ORR activity of Pt–Pd NFs/RGOs [51]. To further evaluate the ORR activity of Pt–Pd NFs/RGOs and commercial Pt–C (50 wt %), the diffusion-limiting current density at 0.30 V were normalized with the loading amount of Pt (Fig. 8B). The Pt–Pd NFs/RGOs modified electrode exhibit a mass activity of 35.3 mA mg^{-1}, higher than that of commercial 50 wt % Pt–C (32.6 mA mg^{-1}), manifesting the enhanced catalytic activity of Pt–Pd NFs/RGOs [52].

An additional important index for ORR is the electron transfer kinetics and thereby a series of polarization curves were performed at different rotating rates in O_2-saturated 0.5 M H_2SO_4 (Fig. 8C). For the Pt–Pd NFs/RGOs modified electrode, the Koutechy–Levich plots (Fig. 8D) are obtained based on the diffusion limiting current densities taken at 0.1 (curve a) and 0.3 V (curve b). The ORR performances in the diffusion limited regions are analyzed by the Koutechy–Levich equation [5,53]. The electron-transfer number (n) is about 4.06 and 4.08 at the potentials of 0.1 and 0.3 V, respectively, indicating that the catalytic reduction of O_2 to H_2O is mainly dominated by a four-electron transfer pathway [54].

For the fuel cell applications, the durability of a catalyst has been considered as one of the important points [53,55]. Therefore, cyclic
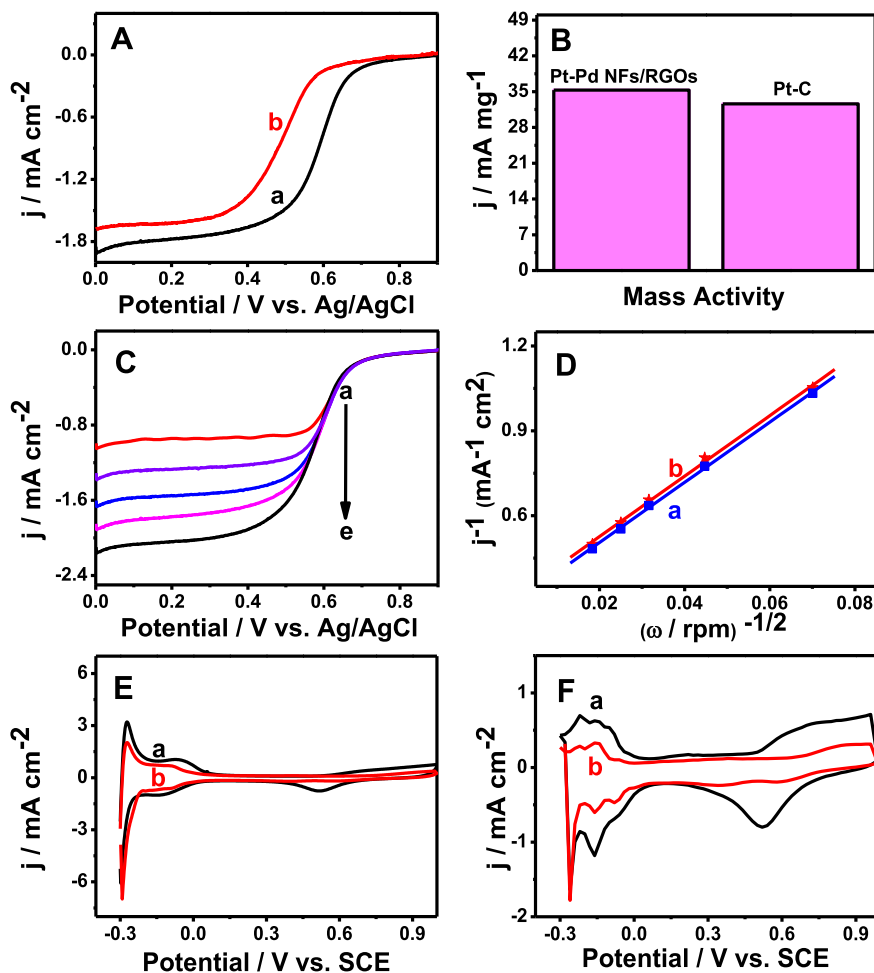

Fig. 8. Current–potential curves (A) of the Pt–Pd NFs/RGOs (curve a) and commercial Pt–C (50 wt %, curve b) modified electrodes in O_2-saturated 0.5 M H_2SO_4 at 5 mV s^{-1} with a rotating rate of 1600 rpm and their corresponding mass activity (B) at 0.30 V. Current–potential curves (C) of the Pt–Pd NFs/RGOs modified electrode with different rotating rates (curve a–e): 200, 500, 1000, 1600, and 3000 rpm. Koutecky–Levich plots (D) for O_2 reduction at 0.1 V (curve a) and 0.3 V (curve b), respectively. Cyclic voltammograms (E and F) of the Pt–Pd NFs/RGOs (curve a) and commercial Pt–C (50 wt %, curve b) modified electrodes in 0.5 M H_2SO_4 before and after 500 cycles at 50 mV s^{-1}, respectively.

voltammograms were recorded for 500 cycles to probe the catalytic durability of the Pt−Pd NFs/RGOs modified electrode in 0.5 M H_2SO_4 (Fig. 8E), using commercial Pt−C (50 wt %) as a reference (Fig. 8F). After 500 cycles, the current densities of Pt−Pd NFs/RGOs and commercial Pt−C (50 wt %) decrease to 67% and 41% in the hydrogen adsorption/desorption region, respectively. Moreover, the hydrogen adsorption peak is negatively shifted with a value of 23 mV for Pt−Pd NFs/RGOs, smaller than that of commercial Pt−C (50 wt %) with a negative shift of 34 mV. These results confirm well durability of Pt−Pd NFs/RGOs [4,56].

As known, a common ORR process involves both the breaking of the O−O bond and the formation of the OH bond [57]. Previous work verifies that the d-band center energy (ε_d) of a catalyst plays a key role in determining the surface reactivity [58]. A higher ε_d of Pt-based catalyst tends to facilitate the O−O bond breaking but unfavorably forms the OH bond, inclining to strongly binding adsorbates. Conversely, a lower one can promote the formation of the OH bond while it's weak to bind adsorbates. As a result, the changes of ε_d might be responsible for different ORR activities of various metals. In our case, it's believed that the presence of Pd in Pt−Pd/ RGOs causes the change of ε_d of Pt and the increase of Pt−Pd distance, bring the improved ORR activity, compared with commercial Pt−C (50 wt %). This change can weaken the Pt−O$^-$ adsorption and enhance the ORR kinetics of Pt monolayer, which is similar to those in the literature [37,59]. Besides, the enhanced ORR activity and long-term durability of Pt−Pd NFs/RGOs can also be attributed to the unique flower-like nanostructures for providing more active sites available and fast electron-transfer kinetics of RGOs [31,60,61].

4. Conclusions

In summary, we prepared well-defined Pt−Pd alloyed nano-flowers uniformly supported on RGOs by a simple wet-chemical approach, without using any seed, template, or organic solvent. The as-prepared nanocomposites displayed the enhanced ORR performance mainly by a four-electron transfer pathway and the improved durability. These are due to the synergistic effects between Pt and Pd, abundant catalytic active sites of Pt−Pd NFs, and the unique structures of RGOs as a support for loading catalysts. Compared to individual Pt catalysts, the as-prepared Pt−Pd nano-crystals possess higher electrocatalytic activity with lower synthesis cost (low Pt catalysts), which makes it a fascinating electrocatalyst for fuel cells application. Furthermore, this simple one-pot synthesis strategy opens a new avenue for preparing other functional nanostructures on suitable supporting materials.

Acknowledgments

Appendix A. Supplementary data

Supplementary data related to this article can be found at http:// dx.doi.org/10.1016/j.jpowsour.2014.06.149.

References

[1] X. Bi, R. Wang, Y. Ding, Electrochim. Acta 56 (2011) 10039–10043.
[2] A. Chen, P. Holt-Hindle, Chem. Rev. 110 (2010) 3767–3804.
[3] S. Du, Int. J. Low Carbon Technol. 7 (2012) 44–54.
[4] X. Huang, E. Zhu, Y. Chen, Y. Li, C.-Y. Chiu, Y. Xu, Z. Lin, X. Duan, Y. Huang, Adv. Mater. 25 (2013) 2974–2979.
[5] Z. Jiang, Z.-J. Jiang, X. Tian, W. Chen, J. Mater. Chem. A 2 (2014) 441–450.
[6] Y. Lu, Y. Jiang, W. Chen, Nano Energy 2 (2013) 836–844.
[7] S.-S. Li, J.-J. Lv, Y.-Y. Hu, J.-N. Zheng, J.-R. Chen, A.-J. Wang, J.-J. Feng, J. Power Sources 247 (2013) 213–218.
[8] C. Li, Y. Yamauchi, Phys. Chem. Chem. Phys. 15 (2013) 3490–3496.
[9] C. Cui, L. Gan, H.-H. Li, S.-H. Yu, M. Heggen, P. Strasser, Nano Lett. 12 (2012) 5885–5889.
[10] A. Sarkar, A. Manthiram, J. Phys. Chem. C 114 (2010) 4725–4732.
[11] X. Liu, D. Wang, Y. Li, Nano Today 7 (2012) 448–466.
[12] M. Nesselberger, S. Ashton, J.C. Meier, I. Katsounaros, K.J.J. Mayrhofer, M. Arenz, J. Am. Chem. Soc. 133 (2011) 17428–17433.
[13] R. Wang, Y. Xie, K. Shi, J. Wang, C. Tian, P. Shen, H. Fu, Chem. Eur. J. 18 (2012) 7443–7451.
[14] C.-T. Hsieh, W.-Y. Chen, D.-Y. Tzou, A.K. Roy, H.-T. Hsiao, Int. J. Hydrogen Energy 37 (2012) 17837–17843.
[15] X. Huang, Z. Yin, S. Wu, X. Qi, Q. He, Q. Zhang, Q. Yan, F. Boey, H. Zhang, Small 7 (2011) 1876–1902.
[16] S. Guo, D. Wen, Y. Zhai, S. Dong, E. Wang, ACS Nano 4 (2010) 3959–3968.
[17] C. Tan, X. Huang, H. Zhang, Mater. Today 16 (2013) 29–36.
[18] X. Huang, X. Qi, F. Boey, H. Zhang, Chem. Soc. Rev. 41 (2012) 666–686.
[19] M. Liu, Y. Lu, W. Chen, Adv. Funct. Mater. 23 (2013) 1289–1296.
[20] F. Li, Y. Guo, R. Li, F. Wu, Y. Liu, X. Sun, C. Li, W. Wang, J. Gao, J. Mater. Chem. A 1 (2013) 6579–6587.
[21] W.S. Hummers, R.E. Offeman, J. Am. Chem. Soc. 80 (1958) 13.
[22] L. Wang, Y. Nemoto, Y. Yamauchi, J. Am. Chem. Soc. 133 (2011) 9674–9677.
[23] W. Zhang, M. Wang, J. Chen, T. Romeo, A.T. Harris, A.I. Minett, Electrochem. Commun. 34 (2013) 73–76.
[24] L. Gao, W. Yue, S. Tao, L. Fan, Langmuir 29 (2012) 957–964.
[25] A.C. Ferrari, D.M. Basko, Nat. Nano 8 (2013) 235–246.
[26] X. Feng, R. Li, C. Hu, W. Hou, J. Electroanal. Chem. 657 (2011) 28–33.
[27] B.P. Vinayan, R. Nagar, V. Raman, N. Rajalakshmi, K.S. Dhathathreyan, S. Ramaprabhu, J. Mater. Chem. 22 (2012) 9949–9956.
[28] T.T. Dang, V.H. Pham, B.K. Vu, S.H. Hur, E.W. Shin, E.J. Kim, J.S. Chung, Mater. Lett. 86 (2012) 161–164.
[29] T.V. Cuong, V.H. Pham, Q.T. Tran, S.H. Hahn, J.S. Chung, E.W. Shin, E.J. Kim, Mater. Lett. 64 (2010) 399–401.
[30] J. Zhang, H. Yang, G. Shen, P. Cheng, J. Zhang, S. Guo, Chem. Commun. 46 (2010) 1112–1114.
[31] X.-R. Li, X.-L. Li, M.-C. Xu, J.-J. Xu, H.-Y. Chen, J. Mater. Chem. A 2 (2014) 1697–1703.
[32] G. Sourov, K.S. Ranjan, C.R. Raj, Nanotechnology 23 (2012) 385602–385610.
[33] S.K. Meher, G.R. Rao, J. Phys. Chem. C 117 (2013) 4888–4900.
[34] J.-J. Lv, J.-N. Zheng, S.-S. Li, L.-L. Chen, A.-J. Wang, J.-J. Feng, J. Mater. Chem. A 2 (2014) 4384–4390.
[35] Y.-W. Lee, A.R. Ko, D.-Y. Kim, S.-B. Han, K.-W. Park, RSC Adv. 2 (2012) 1119–1125.
[36] K.P. Pramoda, H. Hussain, H.M. Koh, H.R. Tan, C.B. He, J. Polym. Sci. Part A Polym. Chem. 48 (2010) 4262–4267.
[37] G. Fu, K. Wu, J. Lin, Y. Tang, Y. Chen, Y. Zhou, T. Lu, J. Phys. Chem. C 117 (2013) 9826–9834.
[38] L. Shi, A. Wang, T. Zhang, B. Zhang, D. Su, H. Li, Y. Song, J. Phys. Chem. C 117 (2013) 12526–12536.
[39] L. Shi, A. Wang, Y. Huang, X. Chen, J.J. Delgado, T. Zhang, Eur. J. Inorg. Chem. 2012 (2012) 2700–2706.
[40] X. Huang, Y. Li, Y. Li, H. Zhou, X. Duan, Y. Huang, Nano Lett. 12 (2012) 4265–4270.
[41] Y. Lu, Y. Jiang, H. Wu, W. Chen, J. Phys. Chem. C 117 (2013) 2926–2938.
[42] J.-J. Lv, J.-N. Zheng, Y.-Y. Wang, A.-J. Wang, L.-L. Chen, J.-J. Feng, J. Power Sources 265 (2014) 231–238.
[43] A. Essalik, K. Amouzegar, O. Savadogo, J. Appl. Electrochem. 25 (1995) 404–407.
[44] D.J.L. Brett, S. Atkins, N.P. Brandon, V. Vesovic, N. Vasileiadis, A.R. Kucernak, J. Power Sources 133 (2004) 205–213.
[45] M.J. Watt-Smith, J.M. Friedrich, S.P. Rigby, T.R. Ralph, F.C. Walsh, J. Phys. D Appl. Phys. 41 (2008) 174004.
[46] C. Hu, Z. Bai, L. Yang, J. Lv, K. Wang, Y. Guo, Y. Cao, J. Zhou, Electrochim. Acta 55 (2010) 6036–6041.
[47] W.H. Lee, H. Kim, Int. J. Hydrogen Energy 38 (2013) 7126–7132.
[48] C. Hu, Y. Guo, J. Wang, L. Yang, Z. Yang, Z. Bai, J. Zhang, K. Wang, K. Jiang, ACS Appl. Mater. Interfaces 4 (2012) 4461–4464.
[49] L. Wang, Y. Yamauchi, Chem. Mater. 21 (2009) 3562–3569.
[50] M. Wang, W. Zhang, J. Wang, A. Minett, V. Lo, H. Liu, J. Chen, J. Mater. Chem. A 1 (2013) 2391–2394.
[51] L. Xiong, Y.-X. Huang, X.-W. Liu, G.-P. Sheng, W.-W. Li, H.-Q. Yu, Electrochim. Acta 89 (2013) 24–28.
[52] S.M. Alia, K.O. Jensen, B.S. Pivovar, Y. Yan, ACS Catal. 2 (2012) 858–863.
[53] C. Hsu, C. Huang, Y. Hao, F. Liu, Phys. Chem. Chem. Phys. 14 (2012) 14696–14701.
[54] M. Shao, A. Peles, K. Shoemaker, Nano Lett. 11 (2011) 3714–3719.
[55] S.-S. Li, J.-N. Zheng, X. Ma, Y.-Y. Hu, A.-J. Wang, J. Chen, J.-J. Feng, Nanoscale 6 (2014) 5708–5713.
[56] C. Koenigsmann, A.C. Santulli, K. Gong, M.B. Vukmirovic, W.-P. Zhou, E. Sutter, S.S. Wong, R.R. Adzic, J. Am. Chem. Soc. 133 (2011) 9783–9795.

[57] A. Morozan, B. Jousselme, S. Palacin, Energy Environ. Sci. 4 (2011) 1238—1254.
[58] H. Zhang, Y. Yin, Y. Hu, C. Li, P. Wu, S. Wei, C. Cai, J. Phys. Chem. C 114 (2010) 11861—11867.
[59] W. He, J. Liu, Y. Qiao, Z. Zou, X. Zhang, D.L. Akins, H. Yang, J. Power Sources 195 (2010) 1046—1050.
[60] D. Wang, H.L. Xin, Y. Yu, H. Wang, E. Rus, D.A. Muller, H.D. Abruña, J. Am. Chem. Soc. 132 (2010) 17664—17666.
[61] X. Chen, B. Su, G. Wu, C.J. Yang, Z. Zhuang, X. Wang, X. Chen, J. Mater. Chem. 22 (2012) 11284—11289.